Theoretical and Applied Fracture Mechanics 90 (2017) 154–164

Contents lists available at ScienceDirect

Theoretical and Applied Fracture Mechanics

journal homepage: www.elsevier.com/locate/tafmec

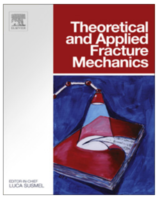

# Mesoscale fracture of a bearing steel: A discrete crack approach on static and quenching problems

Diego Said Schicchi [a,*], Antonio Caggiano [b,c], Santiago Benito [d], Franz Hoffmann [a]

[a] Stiftung Institut für Werkstofftechnik (IWT), Bremen, Germany
[b] INTECIN, Facultad de Ingeniería, Universidad de Buenos Aires and CONICET, Argentina
[c] Institut für Werkstoffe im Bauwesen, Technische Universität Darmstadt, Germany
[d] Universidad Tecnológica Nacional FRBA, Argentina and Ruhr-Universität Bochum, Germany

ARTICLE INFO

*Article history:*
Received 16 January 2017
Revised 6 April 2017
Accepted 18 April 2017
Available online 20 April 2017

*Keywords:*
Fracture
Interface model
Quench cracking
Mesoscale
100Cr6

ABSTRACT

A discontinuous approach aimed at modeling the brittle fracture behavior of mesoscopic 100Cr6 (SAE 52100) steel specimens is presented in this work. The proposal accounts for explicitly considering carbide particles and martensitic matrix in a metallographic image based mesoscale model. Two-dimensional numerical tests are carried out for the mesoscale specimens including a temperature dependent elasto-plastic matrix dealing with the martensitic/austenitic phases and the embedded elastic carbide particles. A fracture damage-based interface constitutive rule is then employed for modeling the brittle behavior occurring at the joint between both the carbides-to-matrix and the matrix-to-matrix interfaces. The soundness and capability of the proposed formulation dealing with the quench cracking phenomenon is demonstrated. Experimental tensile test results on a 100Cr6 steel in its martensitic phase, at room and high temperature, are employed and the evaluation of microcracks formation during a High-Speed-Quenching test is also discussed.

## 1. Introduction

Fracture processes in metals dealing with the separation of a body into two or more pieces due to external actions is a complex phenomenon largely investigated in the literature [1]. Steps of fracture are typically two: (i) crack formation and (ii) crack propagation. It is depending on the ability of the material to develop deformations and plastic strains, before failure, that two fracture modes can be defined. They are recognized in the literature as "ductile" and "brittle" fracture [2]. On the one hand, brittle fracture includes both cleavage phenomena and inter-layer/granular cracks and separations. Brittle response is typically characterized by a low toughness response of the material: the process accounts for relatively small plastic deformations and the crack propagation is highly unstable and rapid [3]. On the other hand, ductile fracture deals with cavitation growing and extensive plastic deformation ahead of cracking: fracture is more stable and capable to resist further strains and displacements under applied stress with a remarkable toughness and strain hardening response [4].

Plenty of investigations have gained increasing interest modeling the ductile fracture behavior in metals. Numerical models available in the literature tried to describe the ductile fracture, mainly accounting for the processes typically occurring at the microscopic standpoint; such as the nucleation, growth and coalescence of voids [5,6]. The majority of the proposals are classically represented by a modified version or extension of a model originally developed by Gurson [7]. Based on this, Tvergaard and Needleman [8] developed a constitutive model which accounted for a damage accumulation induced by nucleation, growth and coalescence of voids through suitable porosity-based internal rules. This model is classical referred nowadays as the GTN (Gurson-Tvergaard-Needleman) model and is typically employed to describe both plasticity and ductile fracture in porous materials and metals. Outstanding extensions of the GTN model have been recently proposed for studying ductile fractures under high and low stress triaxiality [9], for determining the forming limit curve of anisotropic sheet metals [10] and for analyzing the edge crack behavior of steel sheet in multi-pass cold rolling [11]. Further original applications deal with the combination of the GTN model with eXtended-FEM for investigating the crack propagation in ductile materials [12] or a multiscale procedure where the constituents of the nanocomposites were governed by the GTN damage criterion [13].

Under micro and mesoscale levels of observation, the increasing damage of the material gives rise to the development of

---

* Corresponding author.
*E-mail address:* schicchi@iwt-bremen.de (D. Said Schicchi).

http://dx.doi.org/10.1016/j.tafmec.2017.04.006
0167-8442/© 2017 Elsevier Ltd. All rights reserved.

discontinuous cracks, representing first order displacement discontinuities which, e.g. in some steels, can evolve at interfaces of second phase particles and inclusions of the material under consideration. These processes, developed without formation of plastic (localized) strains, represent the brittle fracture case. The methodologies adopted in the literature for brittle fracture mainly followed the so-called "local approach" which was originally developed within the Beremin model [14]. Recent developments in brittle and quasi-brittle failure assessment of engineering materials by means of local approaches have been outlined in [15]. The application of a local approach for investigating the brittle fracture of a reactor's pressure vessel steel has been proposed by Forget et al. [16]. The prediction of fracture toughness in ductile-to-brittle transition region using combined Beremin model (for cleavage phenomena) and a continuum damage mechanics model by Bonora et al. [17] (for ductile tearing) is reported in Moattari et al. [18]. In addition, recent developments in the scientific community are represented by the application of the phase-field method to the prediction of dynamic fracture of brittle and ductile materials as figured out in [19,20].

On the other hand, it is highlighted that, despite of all research made during the last decades on different materials and quenchants regarding residual stresses, distortions and cracking, the generation and propagation mechanisms of quench cracks are still not completely understood at microscopic level [21,22]. Moreover, the quench cracking phenomenon has been deeply studied experimentally [23–25], but also simulations have been used in order to clarify it [26–28]. However, all the available studies in the literature were made at the macroscale, and no influence of the real microstructure (carbides, segregations, etc.) has been taken into account.

In this work, in the framework of the local approach, a mesoscale procedure is proposed for investigating the brittle fracture of 100Cr6 steel. The predictions of the numerical model are evaluated at mesoscopic scale whereby martensitic/austenitic matrix and carbides are differentiated. Furthermore, a fracture damage-based interface constitutive rule deals with the modeling of the brittle fracture behavior occurring at both joint types, meaning: the (i) carbide particles/matrix and the (ii) matrix/matrix interfaces; having a martensitic matrix only for the proposed tensile tests, and an austenitic/martensitic matrix for the case of the quenching problem.

Incorporating a new approach dealing with the quench cracking considering the real microstructure of the material is the main contribution of this work to the current state-of-the-art.

After the above introduction, the paper is organized as follows. Section 2 outlines the procedure for the mesoscale geometry generation and the assumptions for analyzing the 100Cr6 steel specimens. Section 3 summarizes the general formulation and basic assumptions of the constitutive models employed in this paper. Section 4 figures out an overview of the experimental campaign and test data employed to calibrate and validate the model performance. Then, Section 5 deals with the model calibration, numerical results and comparisons. Finally, some concluding remarks are presented in Section 6.

## 2. Mesoscale: main assumptions and geometry

The mesoscale approach proposed in this work deals with a polygonal representation of coarse particles (carbides), which are embedded in a surrounding matrix representing the austenitic/-martensitic phase, in bearing steel specimens. The mesoscale geometry was obtained from metallographic analyses performed on the tested specimen and considering a region where a microcrack was found. The detailed process is described in Section 4 with further details.

The quenched 100Cr6 steel microstructure, shown in Fig. 1, is considered in this study. Additionally, it is remarked that in order to evaluate the mesoscopic behavior in a first attempt, as it has been assessed by other researchers [29–31], an a priori representative geometry based on metallographic analysis has been selected for the study.

In order to isolate the particles from the matrix, seeking to obtain their distribution, position and the basic topology of the polygons, five steps were followed. Those were:

1. Obtaining a micrograph of the 100Cr6 steel specimen with the appropriate magnification and scale of interest.
2. Uploading the micrograph image into a raster graphics editor software and, subsequently, selecting a region representative of the mesoscale (considering the particles distribution).
3. Converting the mesoscale image (rastered in the above step) into a binary file (in MATLAB®).
4. Extracting the interfaces between the two phases (carbides and martensite) as a CAD file using a vector graphics editor software.
5. Importing the CAD file (containing particles, matrix and interfaces) in the CAE software and creating the mesogeometry for the numerical analyses.

The procedure above described allowed to recognize the two phases under consideration, i.e., the martensitic matrix and carbides particles as can be seen in the micrograph of Fig. 1, where the selected representative area of the quenched specimen (having a dimension of $30 \times 30\ \mu m^2$) is proposed. Starting from this selected region of the micrograph (Fig. 2a), the generated high contrast image of the involved particles is presented in Fig. 2b.

The resulting black and white image (Fig. 2b) was then imported in MATLAB® and converted to a square numerical matrix, in which the matrix size corresponded to the horizontal and vertical pixels defining the image. In each entry of the matrix an 8-bit value containing the RGB color information of each pixel was stored. After this, a binary conversion of the image was done adopting "0" and "1" for the black and white colors, replacing the pixel information in the composite specimen. As the image already had high contrast between the phases, the threshold value was automatically and easily defined by MATLAB® Image Processing Environment.

Once the binary image was created, the carbides having a mean diameter lower than $0.33\ \mu m$ (approximately $0.09\ \mu m^2$ or 29 pixels) were removed from the image. This permits to simplify the mesoscale geometry and the subsequent mesh size of the problem (see Fig. 3). It is worth mentioning that previous works [32,33] outline that very small carbides showed no influence on the mesoscale fracture behavior for this same steel. Therefore, they are not considered in the current static and quenching mesoscale simulations. Fig. 4 deals with a comparison between the original and modified particles distribution. It demonstrates that no considerable perturbation can be observed with the adopted modification. Particularly, the original (with all carbides) and the modified (after removing the aforementioned small particles) density distributions show no significant difference among them.

Making use of a vector graphics editor the boundaries between carbides and matrix were extracted from the binary image. The vectorization of the original raster image was automatically performed with good stability due to the high contrast between carbides and matrix. Thus, the resulting vector image containing the borders was exported as a CAD file in the form of nonuniform rational B-splines (NURBS) curves. Finally, from the splines objects

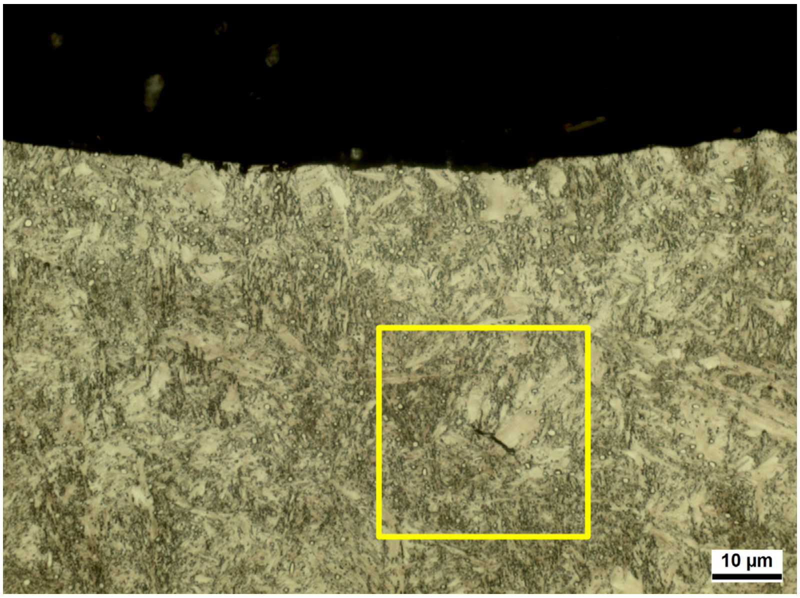

**Fig. 1.** Chosen micrograph and selected area for image processing.

(using Abaqus®) different parts were created, one for each carbide and several partitions of the corresponding matrix, in order to define contacts in all these interactions (see Fig. 5), necessary to capture arbitrary fractures in the mesoscale specimen through the matrix.

Once the mesoscale geometry was obtained, the generation of a Finite Element (FE) mesh for the simulation of the fracture behavior of the considered heterogeneous material could be finally performed.

## 3. Constitutive models involved in the numerical simulations

The constitutive models for the FE simulations of mesoscale fracture in bearing steel specimens are presented in this section. The main goal of this article is to model fracture processes based on a discrete crack approach for both tensile tests and microcracks generated during quenching, on the martensitic phase. For this purpose, a general description of the quenching problem is described in this section, since the tensile test simulation can be considered as a particular case of this general coupled metallo-thermo-mechanical problem.

### 3.1. Coupled metallo-thermo-mechanical equations of continuous media

This section outlines the constitutive models of continuous elements accounting for coupled metallo-thermo-mechanical actions occurring during quenching.

#### 3.1.1. Heat conduction problem and phase transformation

The heat conduction equation, describing the body temperature distribution, is given by

$$\rho c_p \frac{\partial T}{\partial t} = \nabla \cdot (k \nabla T) + \dot{q}_v \tag{1}$$

being $T$ the temperature, $t$ the time, $k = k(T)$ the temperature dependent thermal conductivity, $\rho = \rho(T)$ the density and $c_p = c_p(T)$ the heat capacity. $\nabla \cdot$ and $\nabla$ represent the divergence and gradient tensor operators, respectively.

The latent heat of the phases transformation (source term) is described through the following relationship

$$\dot{q}_v = \sum_i \Delta H_i \, \dot{\xi}_i \tag{2}$$

with $\Delta H_i$ the transformation enthalpy per unit volume of the $i$-th phase and $\dot{\xi}_i$ the $i$-th phase transformation rate.

The (natural) boundary conditions at the surface are given by

$$-k \frac{\partial T}{\partial n} = h\left(T - T_q\right) \tag{3}$$

where $h$ is the heat transfer coefficient, $T_q$ the temperature of the quenching medium and $\partial T / \partial n$ is the directional derivative of the temperature in the outer normal direction.

The initial (temperature) condition for the whole part is given by

$$T(t = 0) = T_0. \tag{4}$$

The martensitic transformation occurring during quenching is accounted by means of the Koistinen-Marburger model [34] outlined in the following

$$\xi_M = \xi_A (1 - \exp\left[-b\,(M_S - T)\right]) \tag{5}$$

being $\xi_M$ and $\xi_A$ the martensite and austenite volume fraction, respectively, $M_S$ the martensite start temperature and $b$ a material parameter.

#### 3.1.2. Thermo-mechanical problem

The mechanical behavior, considering the problem as quasi-static, is governed through the following equilibrium equation

$$\nabla \cdot \boldsymbol{\sigma} + \rho \boldsymbol{b} = \mathbf{0} \tag{6}$$

where $\boldsymbol{\sigma}$ is the Cauchy stress tensor and $\rho \boldsymbol{b}$ represents the vector of body forces.

During a heat treatment problem the strain rate equilibrium at any point at a time $t$ is given by

$$\dot{\varepsilon}_{ij} = \dot{\varepsilon}^{e}_{ij} + \dot{\varepsilon}^{p}_{ij} + \dot{\varepsilon}^{th}_{ij} + \dot{\varepsilon}^{pt}_{ij} + \dot{\varepsilon}^{tp}_{ij} \tag{7}$$

where $\dot{\varepsilon}_{ij}$, $\dot{\varepsilon}^{e}_{ij}$, $\dot{\varepsilon}^{p}_{ij}$, $\dot{\varepsilon}^{th}_{ij}$, $\dot{\varepsilon}^{pt}_{ij}$ and $\dot{\varepsilon}^{tp}_{ij}$ are the total, elastic, plastic, thermal, isotropic phase transformation and transformation plasticity strain rate tensors (here expressed in components $_{ij}$), respectively. A detailed explanation of their calculation and the numerical implementation is assessed in [35].

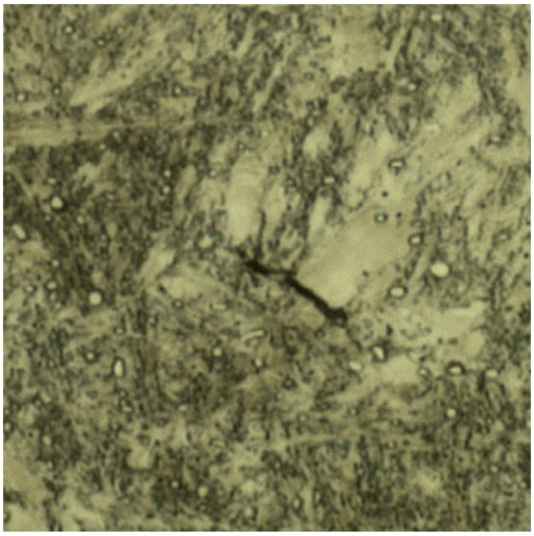

(a) Selected area for image analysis.

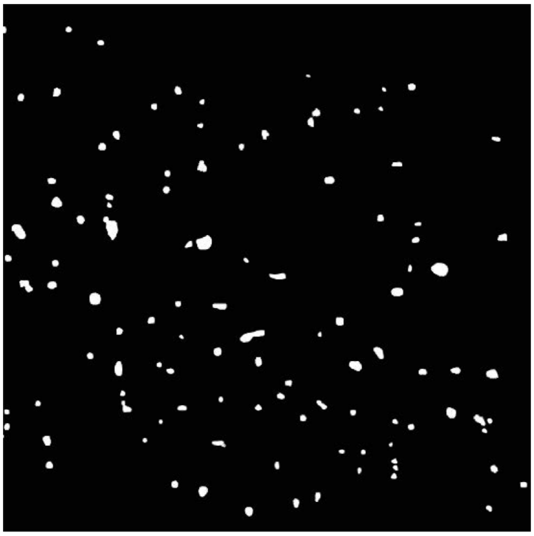

(b) High contrast image of the carbides and matrix.

**Fig. 2.** Mesoscale geometry pre-processing.

A parenthesis is made in order to remark that the tensile tests on martensitic specimens deal with $\dot{\varepsilon}^{th}_{ij} = 0$ due to the constant temperature, and $\dot{\varepsilon}^{pt}_{ij} = \dot{\varepsilon}^{tp}_{ij} = 0$ since there are no phase transformations.

Concerning the classical plasticity, a *strain hardening transmission* model regarding the so-called "*memory effect*" [36,37] has been employed for the diffusionless martensitic transformation; i.e. full memory is considered to exist.

Hence, the incremental stress-strain relation for the elasto-plastic material model can be written as

$$\begin{aligned} \dot{\varepsilon}^{e}_{ij} &= E^{-1}_{ijkl}\dot{\sigma}_{kl} \\ \dot{\sigma}_{ij} &= E_{ijkl}\left(\dot{\varepsilon}_{kl} - \dot{\varepsilon}^{p}_{kl} - \dot{\varepsilon}^{th}_{kl} - \dot{\varepsilon}^{pt}_{kl} - \dot{\varepsilon}^{tp}_{kl}\right) \end{aligned} \qquad (8)$$

being $\boldsymbol{E}$ the fourth-order elasticity tensor (and $E_{ijkl}$ its components).

The yield function $\phi$ is expressed as:

$$\phi = \frac{3}{2}\boldsymbol{s} : \boldsymbol{s} - \left(\sigma_y\right)^2 \qquad (9)$$

**Fig. 3.** Processed binary image containing carbides with a mean diameter larger than 0.33 μm.

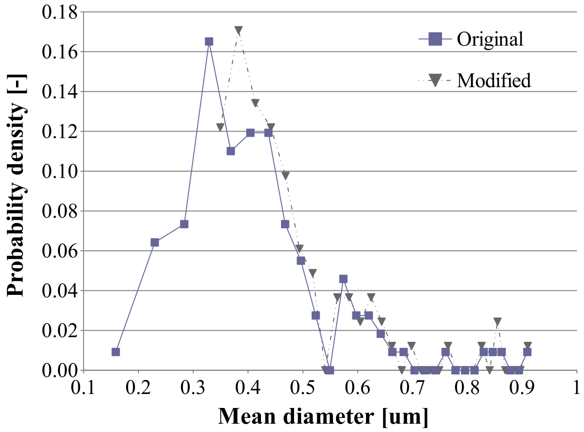

**Fig. 4.** Original and modified (filtered) carbides distributions.

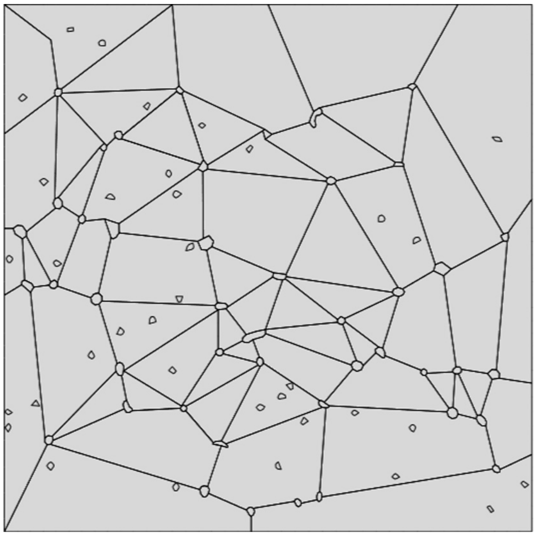

**Fig. 5.** Mesoscale geometry showing the carbide particles, matrix-matrix and carbides-matrix interactions.

being $\boldsymbol{s}$ the deviatoric stress tensor and $\sigma_y = \sigma_y(T, \xi_p, \bar{\varepsilon}^p)$ the yield strength calculated for the mixture of phases.

The classical associated flow rule is employed

$$\dot{\boldsymbol{\varepsilon}}^p = \dot{\lambda}\frac{\partial \phi}{\partial \boldsymbol{\sigma}} \tag{10}$$

where the non-negative plastic multiplier, $\dot{\lambda}$, is derived starting from the classical Kuhn-Tucker loading/unloading (Eq. (11a)) and consistency (Eq. (11b)) conditions

$$\dot{\lambda} \geqslant 0, \phi \leqslant 0, \quad \dot{\lambda}\phi = 0 \tag{11a}$$

$$\dot{\lambda}\dot{\phi} = 0. \tag{11b}$$

Lastly, the following power law is adopted to account for the isotropic hardening of the austenitic and martensitic phases:

$$\sigma_{y_i} = K_i\,(\bar{\varepsilon}^p)^{n_i} \tag{12}$$

where $K_i$ and $n_i$ are the hardening parameter and the hardening exponent of the $i$-th phase, respectively, and $\bar{\varepsilon}^p$ is the equivalent plastic strain.

### 3.2. Coupled thermo-mechanical equations of discontinuous interfaces

Heat transfer throughout interfaces and the coupled fracture-based thermal model for brittle interfaces are outlined in this section. The interface brittle cracking phenomena between the surrounding martensitic phase and carbide inclusions and also between matrix-to-matrix joints have been addressed by means of fracture-based damage interface rules detailed in this subsection.

#### 3.2.1. Interface heat transfer

Heat transfer is governed by means of the following convective rule for interfaces [38,39]

$$q_n = -h_c[|\Delta T|] \tag{13}$$

based on the discontinuity assumption of the temperature field in the contact pair

$$[|\Delta T|] = \left[\left|T^+ - T^-\right|\right] \neq 0 \tag{14}$$

being $h_c$ the heat transfer coefficient, while $T^+$ and $T^-$ are the temperature at the $+$ and $-$ side of the considered interface.

#### 3.2.2. Fracture and temperature based interface model for brittle fracture

This section deals with the temperature dependent interface formulations aimed at modeling brittle fractures. Uncoupled mode I and II energy-based linear damage evolution rules are employed.

The relationship between interface stresses and crack opening displacements is given by means of the following expression

$$\begin{aligned} &\dot{\boldsymbol{u}} = \dot{\boldsymbol{u}}^{el} + \dot{\boldsymbol{u}}^{cr} + \dot{\boldsymbol{u}}^{th} \\ &\dot{\boldsymbol{u}}^{el} = \boldsymbol{C}_d^{-1}\cdot\dot{\boldsymbol{t}} \\ &\dot{\boldsymbol{t}} = \boldsymbol{C}_d\cdot(\dot{\boldsymbol{u}} - \dot{\boldsymbol{u}}^{cr} - \dot{\boldsymbol{u}}^{th}) \end{aligned} \tag{15}$$

where $\dot{\boldsymbol{u}} = [\dot{u}_N, \dot{u}_T]^T$ is the rate of the interface relative displacement vector, which is additively decomposed into the elastic, plastic and thermal components, $\dot{\boldsymbol{u}}^{el}, \dot{\boldsymbol{u}}^{cr}$ and $\dot{\boldsymbol{u}}^{th}$, respectively; $\dot{\boldsymbol{t}} = [\dot{\sigma}_N, \dot{\sigma}_T]^T$ is the stress rate vector, being $\sigma_N$ and $\sigma_T$ the normal and shear components, respectively. Moreover, $\boldsymbol{C}_d$ defines the elastic stiffness matrix,

$$\boldsymbol{C}_d = d_\tau \boldsymbol{C} \qquad \text{with} \quad \boldsymbol{C} = \begin{pmatrix} k_N & 0 \\ 0 & k_T \end{pmatrix} \tag{16}$$

where $k_N$ and $k_T$ are the interface normal and tangential elastic stiffness, respectively, and $d_\tau$ a temperature-dependent scalar parameter.

Following the original proposal by Willam et al. [38], it is assumed that the temperature field can exhibit a jump across the interface due to a strong discontinuity of the interface normal kinematic. The rate of the relative joint displacements due to thermal effects, $\dot{\boldsymbol{u}}^{th}$, is assumed to be linearly related to the rate of the temperature jump across the interface, $\Delta\dot{T}$, through the following relationships

$$\begin{aligned} &\dot{u}_N^{th} = \alpha_s^0\left[\left|\Delta\dot{T}\right|\right] \\ &\dot{u}_T^{th} = \alpha_s^0\left[\left|\Delta\dot{T}\right|\right] \end{aligned} \tag{17}$$

being $\alpha_s^0$ the coefficient of superficial thermal expansion while the norm of the temperature jump (in the interface plane) is indicated as $[|\Delta T|] = \left[\left|T^+ - T^-\right|\right]$ ($T^+$ and $T^-$ are the temperature at the $+$ and $-$ interface sides).

One-dimensional plasticity rules have been considered for the uncoupled normal and shear interface behavior. Particularly, in case of isotropic hardening, the yield condition takes the following form

$$f_{\#} = |\sigma_{\#}| - (\sigma_{\#f} + Q_{\#}) \leqslant 0 \tag{18}$$

being $\sigma_{\#}$ (with $\# =$ "N" or "T" accounting for the normal or tangential components) the interface stress component, $\sigma_{\#f}$ the initial yield stress and $Q_{\#}$ the internal softening variable in post-cracking regime.

The evolution law of $Q_{\#}$ is defined according to the following relation

$$\dot{Q}_{\#} = \dot{\lambda}_{\#}H_{\#} \tag{19}$$

while that of the plastic displacement rate results

$$\dot{u}_{\#}^{cr} = \dot{\lambda}_{\#}\partial f_{\#}/\partial\sigma_{\#} = \dot{\lambda}_{\#}sign[\sigma_{\#}] \tag{20}$$

being $\dot{\lambda}_{\#}$ the plastic multiplier and $H_{\#}$ is the softening modulus.

Finally, the constitutive stress-interface displacement relationship can be written as

$$\begin{pmatrix} \dot{\sigma}_N \\ \dot{\sigma}_T \end{pmatrix} = d_\tau \begin{pmatrix} k_N^{ep} & 0 \\ 0 & k_T^{ep} \end{pmatrix} \begin{pmatrix} \dot{u}_N \\ \dot{u}_T \end{pmatrix} \tag{21}$$

where the elastoplastic continuum tangent moduli $k_{\#}^{ep}$, under loading post-cracking regime, take the form (Fig. 6)

$$k_{\#}^{ep} = \frac{k_{\#}\cdot H_{\#}}{k_{\#} + H_{\#}}. \tag{22}$$

## 4. Experimental input

This section summarizes some experimental data considered as a benchmark with the aim of evaluating the capability and soundness of the proposed model. Particularly, the numerical procedure outlined in Sections 3, 5.1 and 5.2 needs to be validated in its ability to simulate brittle mesoscale fracture processes under both mechanical and coupled thermo-mechanical conditions.

### 4.1. Material

Experimental data, dealing with 100Cr6 steel specimens, was obtained at the Stiftung Institut für Werkstofftechnik in Bremen and reported in the framework of the SFB-570 project [40] in [41,42], among others. Material properties are next summarized

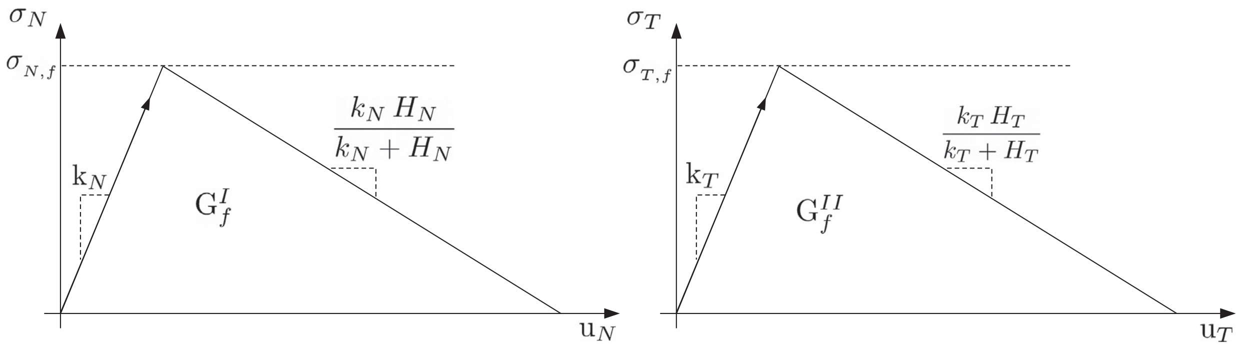

(a) Pure mode I (b) Pure mode II

**Fig. 6.** Interface stress-crack opening relationships.

**Table 1**
Properties of the 100Cr6 steel. Coefficients of the temperature adopted according to the polynomial regression $y = a_0 + a_1 T + \cdots + a_n T^n$ by [41].

| Property | Phase | $a_0$ | $a_1$ | $a_2$ | $a_3$ | $a_4$ |
|---|---|---|---|---|---|---|
| Thermal conductivity [W m$^{-1}$ °C$^{-1}$] | *Martensite* | 4.355E+01 | −1.600E−03 | −4.180E−05 | 1.820E−08 | |
| | *Austenite* | 1.460E+01 | 1.270E−02 | | | |
| Specific heat capacity [J kg$^{-1}$ °C$^{-1}$] | *Martensite* | 4.220E+02 | 9.310E−01 | −2.140E−03 | 2.640E−06 | |
| | *Austenite* | 4.540E+02 | 3.880E−01 | −3.220E−04 | 1.100E−07 | |
| Enthalpie [J kg$^{-1}$] | *Martensite* | 3.820E+03 | 4.220E+02 | 4.660E−01 | −7.130E−04 | 6.600E−07 |
| | *Austenite* | 8.180E+04 | 4.540E+02 | 1.940E−01 | −1.070E−04 | 2.750E−08 |
| Density [kg m$^{-3}$] | *Martensite* | 7.770E+03 | −2.530E−01 | | | |
| | *Austenite* | 8.041E+03 | −5.740E−01 | 2.600E−05 | | |
| Young's modulus [MPa] | *Martensite* | 2.1424E+5 | −8.285E+01 | | | |
| | *Austenite* | 2.6693E+5 | −2.213E+02 | | | |
| Poisson's coefficient [–] | *Martensite* | 3.440E−01 | 1.000E−04 | | | |
| | *Austenite* | 2.230E−01 | 2.500E−04 | | | |
| Hardening exponent [–] | *Martensite* | 1.278E−01 | 8.449E−05 | | | |
| | *Austenite* | 1.092E−01 | | | | |
| Hardening parameter [MPa] | *Martensite* | 5.724E+03 | −6.760E+00 | | | |
| Thermal expansion [10$^{-6}$ °C$^{-1}$] | *Martensite* | 1.090E+01 | | | | |
| | *Austenite* | 2.380E+01 | | | | |

in Table 1. Additionally, the transformation parameters of Eq. (5) are $M_S = 211$ °C and $b = 0.01071$.

Carbides properties were adopted based on [43] by averaging the properties of the different existing particles in this steel (Fe, Cr)$_3$ C type [44,45]). According to this, the considered elastic Young's modulus and Poisson ratio are $E_c = 325$ GPa and $\nu_c = 0.273$, respectively.

### 4.2. Experimental setup

Two kinds of results are simulated and compared in Section 5. On the one hand, tensile tests on martensitic state were performed at both Room (RT) and high temperature. On the other hand, a High-Speed Quenching test on a cylindrical specimen was performed.

#### 4.2.1. Tensile tests

Tensile tests for the martensitic phase were realized at both RT and 200 °C. Specimens with a geometry according to Fig. 7, were firstly gas quenched in a vacuum system, then in a second time cooled down in liquid nitrogen (in order to transform possible remaining retained austenite) and finally tempered for 2 h at 180 °C. Prior to the high temperature test, the specimen was heated in a furnace for 10 min. The tests were performed in an Inspekt 100® machine from Hegewald & Peschke®. The considered tensile strain rate, for all cases, was $4 \times 10^{-3}$ s$^{-1}$. Further details of the experimental campaign have been deeply discussed by Acht et al. [41].

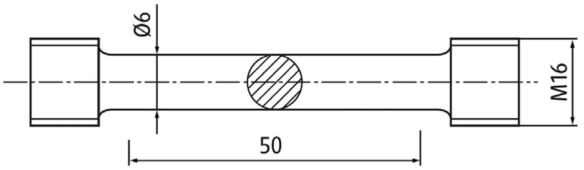

**Fig. 7.** Tensile test specimen and geometry.

#### 4.2.2. High speed quenching test

A cylindrical specimen with a diameter $d = 25$ mm and length $l = 150$ mm was tested in a High-Speed Quenching facility (Fig. 8). Water at room temperature was used as quenchant. The flow was axial to the specimen in the top-down direction. The pumped flow was 16 l/s, which results in a heat transfer coefficient $h = 35$ kW m$^{-2}$ K$^{-1}$ [46]. It is worth noting that there is no temperature dependency of the heat transfer coefficient for this kind of process. This is grounded in the fact that the large quenchant flow (mean velocity in the range of 5–10 m/s) causes a convective heat transfer mechanism only, i.e. no film nor nucleate boiling stages are observed, as commonly occurs in immersion quenching [47].

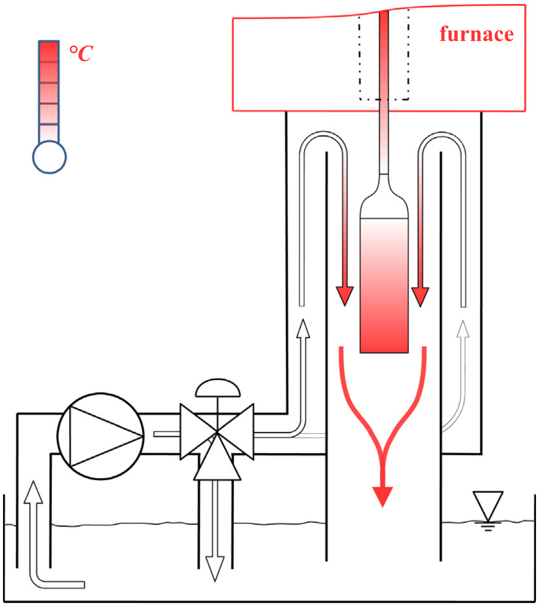

**Fig. 8.** Schematic test set-up of the High-Speed Quenching facility.

The heating was performed in a furnace located just above the cooling device. When austenitizing was finished (900 °C for 50 min), the specimen was rapidly moved down into the center of the quenching device. As soon as the specimen reached its right position, the water flow (up to this point bypassed into the tank) along the quenching device started. A cap of the same base diameter of the specimen was used for flow guidance in order to avoid vortex formation at the top of the probe. Further details of the quenching tests are omitted for the sake of brevity, however a deep discussion of the test set-up and results are reported in Said Schicchi et al. [32].

## 5. Numerical results and comparisons

The numerical examples presented in this section are intended to demonstrate the model capability of capturing the quench microcracking phenomenon based on a discrete-based mesoscale approach. With this purpose, the simulations for tensile tests are firstly discussed. The obtained results, and the concerning model calibration of the discontinuous constitutive model, are then used on the second part of this section, i.e., for the mesoscale quenching problem.

The mesh of the mesoscale geometry (in all the calculations) was formed by 8484 nodes and 6077 3-node linear (generalized plane strain) elements (see Fig. 9). Carbide particles, having a mean diameter lower than 0.43 μm (approximately 0.15 $\mu m^2$ or 50 pixels), were embedded into the surrounding 100Cr6 matrix. Particularly, the nodal degrees of freedom of the carbide elements were eliminated and constrained to the interpolated values of the corresponding surrounding nodes belonging to the matrix element. This technique allowed to simplify and reduce the size of the mesh.

### 5.1. Tensile tests on martensitic state at room and high temperature

In this section, the predictions of the mesoscale model procedure for brittle steels are evaluated whereby martensite matrix and carbide particles are numerically differentiated. The mesoscale geometry above described is employed for investigating the mesoscale fracture behavior of tensile tests against experimental tests reported in Section 4.2.1. A convex polygonal representation of the particles was adopted and symmetry was assumed in the left and bottom sides of the geometry while a displacement-controlled loading was imposed in the top surface of the probe (see Fig. 9).

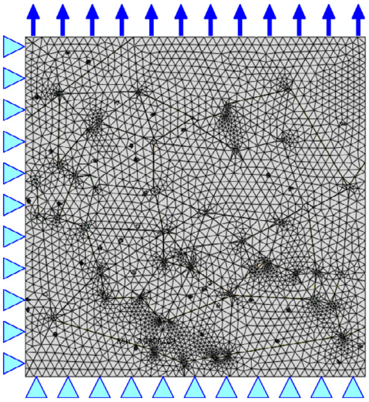

**Fig. 9.** Schematic representation of the mesoscale mesh and boundary conditions for the tensile test problem.

The continuous matrix material properties correspond to the above described in Section 4.1. Then, continuum carbide elements were assumed as linear elastic, whereas all fracturing non-linearities were considered through both the continuous matrix and the zero-thickness interface elements. The latter are defined throughout the adjacent edges of the continuous elements. Non-linear constitutive rules were introduced in those elements according to the formulations outlined in Section 3. As result of the model calibration, the mechanical parameters of the discontinuous rules, employed in the numerical evaluations, are summarized in Table 2. These are next used in the quenching calculation in order to account for the failure in the martensitic state. Further, the temperature dependent normal interface stiffness $k_N$, for both the austenitic and the martensitic phases, was assumed proportional to the Young's modulus (Table 1) of each phase, and estimated dividing the respective values by a coefficient representing the "interface thickness" (0.01 mm in this case). Additionally, based on experimental results, it is considered that the failure starts in the martensitic phase. This is the main reason why the joint behavior for the austenitic phase is assumed as linear elastic and no value for the specific fracture energy is reported.

Figs. 10 and 11 illustrate the cracked configurations at several stages as obtained in the numerical tests at room and high temperature. On the one hand, failure process led to only one macro-crack for the case of tensile tests at RT. It can be observed that in this case the crack evolved in an almost horizontal direction (mode I type of fracture) and only small inclined crack paths can be found as result of the explicitly defined mesostructure of the specimen. On the other hand, two (and less pronounced) cracks can be recognized for the tensile tests at high temperature. Macro-cracks in both examples were predominant in post-elastic softening regime and their evolution tried to evolve along inclusion-matrix interfaces, which in fact represent the weakest part of the specimen.

Finally, numerical results in terms of true stress and strain confirmed the predictive capacity of the model formulation for analyzing the tensile response of 100Cr6 (SAE 52100) steel specimens regarding both failure behavior and failure modes.

### 5.2. Quench cracking numerical tests

A numerical approach with its main focus placed on the study of microcracks formation influenced by second phase particles was introduced by some of the Authors in [32,33,48] and it is here slightly modified in order to work with the current mesoscale

**Table 2**
Calibrated parameters for the zero-thickness interface elements in tensile tests. The temperature range [300–900 °C] corresponds to the austenitic phase.

| Temp. [°C] | $k_N$ [Pa m$^{-1}$] | $k_T$ [Pa m$^{-1}$] | $\sigma_{Nf}$ [MPa] | $\sigma_{Tf}$ [MPa] | $G_I^f = G_{II}^f$ [Pa m$^{-1}$] |
|---|---|---|---|---|---|
| 20 | $2.12 \times 10^7$ | $1.06 \times 10^7$ | 2490 | 1245 | 150 |
| 200 | $2.00 \times 10^7$ | $1.00 \times 10^7$ | 1750 | 875 | 150 |
| 300 | $2.00 \times 10^7$ | $1.00 \times 10^7$ | – | – | – |
| 400 | $1.78 \times 10^7$ | $8.90 \times 10^6$ | – | – | – |
| 500 | $1.56 \times 10^7$ | $7.80 \times 10^6$ | – | – | – |
| 600 | $1.34 \times 10^7$ | $6.70 \times 10^6$ | – | – | – |
| 700 | $1.12 \times 10^7$ | $5.60 \times 10^6$ | – | – | – |
| 800 | $9.00 \times 10^6$ | $4.50 \times 10^6$ | – | – | – |
| 900 | $6.80 \times 10^6$ | $3.40 \times 10^6$ | – | – | – |

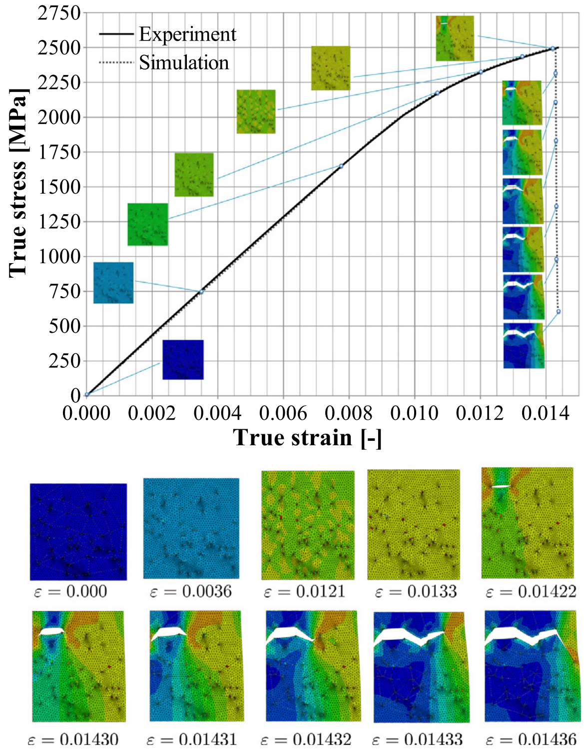

**Fig. 10.** Tensile test at room temperature of 100Cr6 in martensitic state.

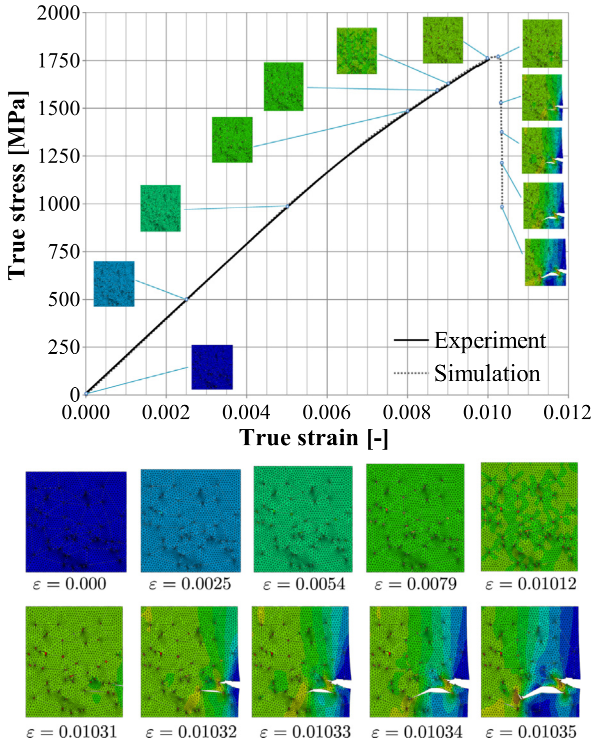

**Fig. 11.** Tensile test at high temperature (200 °C) of 100Cr6 in martensitic state.

model. The main difference lies in the method employed to account for the fracture modeling. In particular, the original proposal adopted the discontinuous X-FEM technique for capturing cracks and/or displacement jumps into the mesoscale specimen; contrarily in this work the discrete approach is based on the use of zero-thickness interfaces. Nonetheless, the main strategy of the thermo-mechanical coupling, macroscale calculation and all other aspects concerning the original model are summarized as follows:

- Firstly, a FE based macroscopic simulation of the High-Speed-Quenching process is done with a 2D-axisymmetric model (same radius and half the length of the specimen is considered due to symmetry).
- Secondly, based on the above macroscopic simulation, numerical results corresponding to stress tensor components, the martensitic/austenitic phase fraction and temperature evolution in time are extracted and stored in a text file for the selected locations.
- Lastly, the FE mesoscale analysis is performed using the extracted curves as boundary conditions in the adopted mesoscale geometry.

A general scheme of the above described strategy can be seen in Figs. 12 and 13. However, further details can be found in the work by Said Schicchi et al. [32].

It is worth noting that the results discussed in the original proposal [32] and further works [33,48] were really satisfactory. Nonetheless, as it was briefly discussed in the introductory section, despite of all the research made during the last decades the quench cracking phenomenon is still not fully (microscopically) understood. That been said, the Authors believe that is really important to increase the efforts in this field, incorporating different techniques and approaches in order to gain a better understanding of this failure mode in a lower scale of analysis (micro, meso and multiscale ones).

The chosen location for the analysis, shown schematically in Fig. 12, corresponds to the surface region in a section located at 15 mm from the bottom plane of the cylindrical specimen. Fig. 1 shows a micrograph of this area, from which the mesoscale geometry was constructed. Here is appreciated as well a microcrack connecting big carbides. This location is the one where curves were extracted from the 2D macroscopic axisymmetric simulation. Then, for the mesoscale analysis, the temperature and phase fractions were imposed in time in the whole geometry. Therefore, only

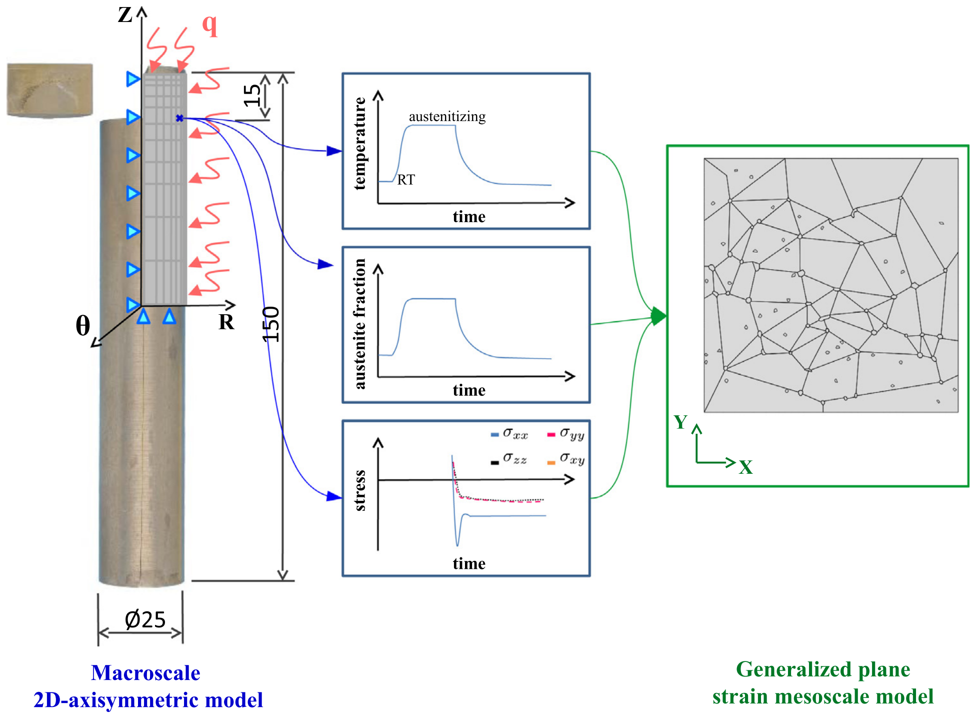

**Fig. 12.** Schematic representation of the 2 stage model strategy.

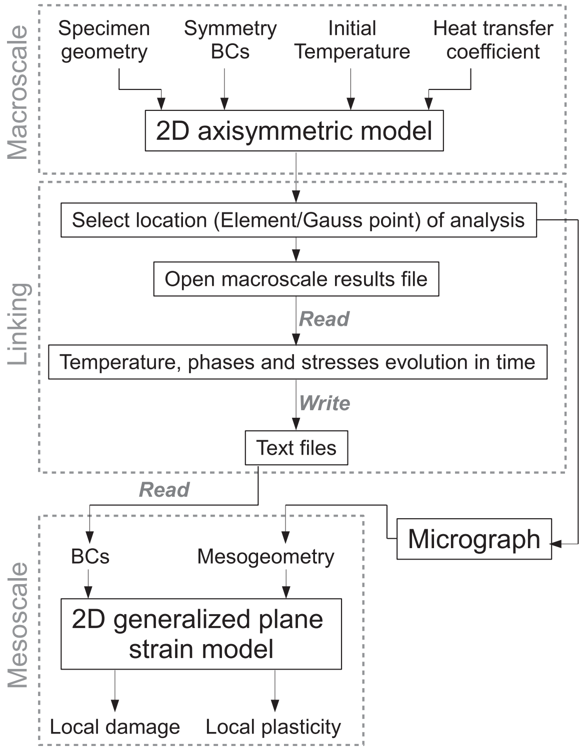

**Fig. 13.** Implemented two-scale solution scheme.

a mechanical problem needs to be solved, using minimal kinematical constraints (or uniform boundary traction) for the displacement problem, where the (extracted) curves of the stress tensor components govern the mesoscale deformation. This condition is given by [49]:

$$\boldsymbol{\sigma}_{\boldsymbol{\mu}}(\boldsymbol{y},t)\cdot\boldsymbol{n}(\boldsymbol{y})=\boldsymbol{\sigma}(t)\cdot\boldsymbol{n}(\boldsymbol{y})\quad\forall\boldsymbol{y}\in\Gamma_{\mu}\tag{23}$$

being $\boldsymbol{\sigma}_{\boldsymbol{\mu}}$ the microscopic stress tensor, $\boldsymbol{n}$ the unit normal vector, $\boldsymbol{y}$ the local coordinate in the boundary $\Gamma_{\mu}$ of the mesoscale geometry and $\boldsymbol{\sigma}$ the macroscopic stress tensor.

As result of these analyses, Fig. 14 presents the equivalent plastic strain field in the matrix material. Particularly, Fig. 14a highlights the clear effect of the particles (specially the larger ones) which act as notches. The observed values are accurately extremelly low, as it is expected for the heating part of the thermal cycle. Fig. 14b reports the final values after quenching and it can be observed the strong effect of the larger particles, concentrating plastic strains in their surrounds. The peak value as shown in Fig. 14b is close to 6%, however this is a local value at a single Gauss point hard to visualize in plain view. Mean value for the plastic strain is $\approx 2.5\%$, which is a perfectly reasonable value for the matrix hardening. Particularly, the diagonal *bottom-left to up-right* exhibits small darker zones with values between 3 and 3.5%. The interaction between particles is observed as well in both cases.

Finally, concerning the fracture response, the damage variable after quenching of the Interface Elements is presented in Fig. 15. The affected zones are in direct correspondence with the locations where larger plastic flow was reached. The propagation of damage across interfaces connecting carbides is also observed in the central region, representing the microcracks in the proximity of large particles and also connecting some of them. These results actually demonstrated the phenomenological capabilities of the mesoscale approach to reproduce qualitatively expected failure (microcracking) during quenching processes. The non-linear model is able to capture the influence of the inclusions on the overall complex thermo-mechanical response.

## 6. Concluding remarks

In the context of brittle fracture modeling, a discrete crack approach was used in this paper to simulate the failure behavior of a bearing steel in martensitic state. Tensile tests at both room

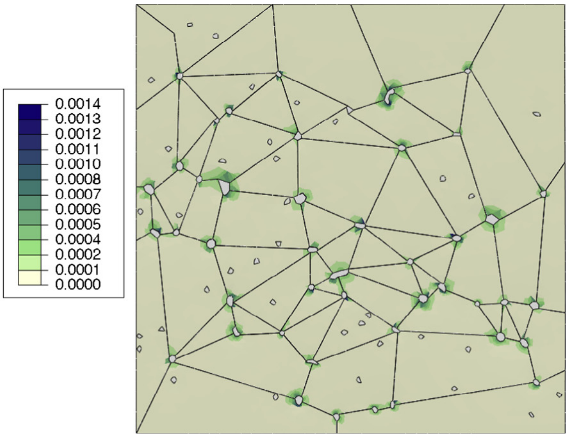

(a) After heating.

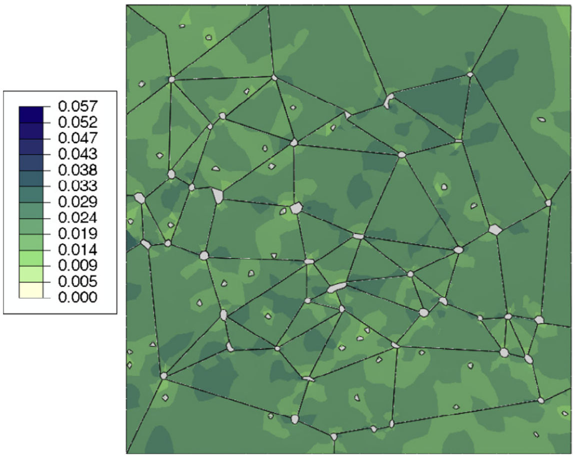

(b) After quenching.

**Fig. 14.** Equivalent plastic strain field.

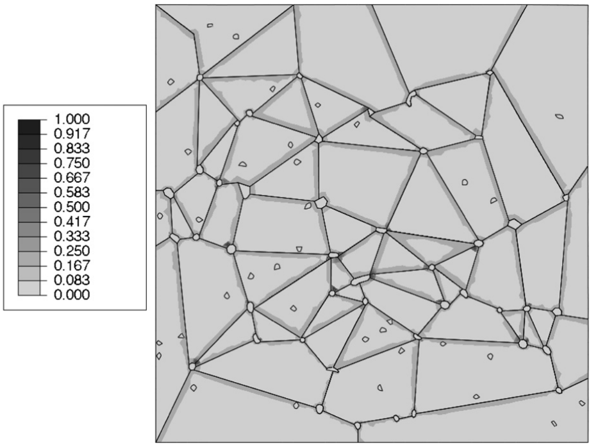

**Fig. 15.** Zones with localized damage after quenching: limits 0 and 1 deals with non-damaged and fully damaged interface states, respectively.

and high temperature and the quench microcracking evolution in a High Speed Quenching test were analyzed by explicitly considering the direct influence of carbide particles and the consequent mesostructure of 100Cr6 (SAE 52100) steel specimens.

A series of final remarks can be drawn out on the basis of both the model formulation and the proposed applications:

- Metallographic image analyses have been used as tool for generating the mesoscale geometry of the multiphase materials under consideration. Geometry aspects, such as shape and size, and distribution of carbide particles were explicitly taken into account with this approach, contrarily to more classical assumptions based on a random distribution of particles (often adopted in available examples of the scientific literature).
- The proposed mesoscale formulation takes into account the composite nature of some brittle materials and the contributions of their various constituents and phases. This formulation is intended as a key element to be possibly employed in numerical models aimed at explicitly simulating the multiphase mechanical behavior of fragile metals.
- The fracture response of the martensitic phase (both at room and high temperature) was well captured by the proposed numerical procedure. The localized damage, initiating at second phase particles, permits to analyze cracking propagation through the matrix material up to the final failure stage.
- The overall results of the proposed two-stage simulation of the quench cracking problem under High-Speed-Quenching conditions showed qualitatively consistency against experimental observations in terms of the generated damage in the surrounds of the carbide particles.

The proposed modeling procedure presented in this article results in a good numerical tool which may be further utilized in order to better understand the mechanical behavior and fracture response at the mesoscopic level of 100Cr6 steel, but also other multiphase materials fracturing in brittle manner. Furthermore, this work represents a novel contribution concerning the quench cracking problem, where there are not currently many available models in the literature which consider the explicit mesoscopic constitution of the material.

Further developments are currently ongoing for better understanding the physics of the mentioned phenomena. Particularly, in this investigation a region of a micrograph was employed to generate the mesoscale geometry of analysis. The authors are currently evaluating the influence on the predictions of different sizes of geometries and different spatial arrangement of heterogeneities as well, following the presented mesoscale approach, and also within the framework of a proper multiscale fracture model under development. In addition, a 3D extension of the present model is also under study looking to avoid the strong assumption of the generalized plane strain simulation made in this work. Moreover, a combined FE - phase field approach to simulate the microstructural evolution during the austenite-to-martensite transformation is planned seeking to study the local effects at the interface between phases. This would allow to better study the effect of retained austenite. Further investigations are also ongoing describing the bond effect between carbides and matrix materials. All these aspects represent the straightforward extension of the model here proposed.

## Acknowledgements

The support of INTI (Instituto Nacional de Tecnología Industrial, Argentina) and Roberto Rocca Education Program, through their respective grants, is gratefully acknowledged by D. Said Schicchi.

## References

[1] A. Pineau, A.A. Benzerga, T. Pardoen, Failure of metals i: brittle and ductile fracture, Acta Mater. 107 (2016) 424–483.
[2] A.J. McEvily, Brittle and ductile fractures, in: Metal Failures: Mechanisms, Analysis, Prevention, second ed., John Wiley & Sons, Inc., 2013, pp. 156–195.
[3] A.H. Cottrell, Theory of brittle fracture in steel and similar metals, Trans. Met. Soc. AIME (1958) 212.

[4] Y. Lou, H. Huh, S. Lim, K. Pack, New ductile fracture criterion for prediction of fracture forming limit diagrams of sheet metals, Int. J. Solids Struct. 49 (25) (2012) 3605–3615.

[5] Y. Lou, H. Huh, Prediction of ductile fracture for advanced high strength steel with a new criterion: experiments and simulation, J. Mater. Process. Technol. 213 (8) (2013) 1284–1302.

[6] D. Said Schicchi, A. Caggiano, A porous-based discontinuous model for ductile fracture in metals, Eng. Fract. Mech. 138 (2015) 19–32.

[7] A.L. Gurson, Continuum theory of ductile rupture by void nucleation and growth: Part i – yield criteria and flow rules for porous ductile media, J. Eng. Mater. Technol. 99 (1) (1977) 2–15.

[8] V. Tvergaard, A. Needleman, Analysis of the cup-cone fracture in a round tensile bar, Acta Metall. 32 (1) (1984) 157–169.

[9] L. Malcher, F.A. Pires, J.C. De Sá, An extended GTN model for ductile fracture under high and low stress triaxiality, Int. J. Plast. 54 (2014) 193–228.

[10] A. Kami, B.M. Dariani, A.S. Vanini, D.S. Comsa, D. Banabic, Numerical determination of the forming limit curves of anisotropic sheet metals using GTN damage model, J. Mater. Process. Technol. 216 (2015) 472–483.

[11] Q. Sun, D. Zan, J. Chen, H. Pan, Analysis of edge crack behavior of steel sheet in multi-pass cold rolling based on a shear modified GTN damage model, Theoret. Appl. Fract. Mech. 80 (2015) 259–266.

[12] J. Crété, P. Longère, J. Cadou, Numerical modelling of crack propagation in ductile materials combining the GTN model and X-FEM, Comput. Methods Appl. Mech. Eng. 275 (2014) 204–233.

[13] S. Song, Y. Chen, Z. Su, C. Quan, V.B. Tan, Multiscale modeling of damage progression in nylon 6/clay nanocomposites, Compos. Sci. Technol. 100 (2014) 189–197.

[14] F. Beremin, A. Pineau, F. Mudry, J.C. Devaux, Y. DEscatha, P. Ledermann, A local criterion for cleavage fracture of a nuclear pressure vessel steel, Metall. Trans. A 14 (11) (1983) 2277–2287.

[15] F. Berto, P. Lazzarin, Recent developments in brittle and quasi-brittle failure assessment of engineering materials by means of local approaches, Mater. Sci. Eng. : R: Rep. 75 (2014) 1–48.

[16] P. Forget, B. Marini, L. Vincent, Application of local approach to fracture of an RPV steel: effect of the crystal plasticity on the critical carbide size, Procedia Struct. Integrity 2 (2016) 1660–1667.

[17] N. Bonora, D. Gentile, A. Pirondi, G. Newaz, Ductile damage evolution under triaxial state of stress: theory and experiments, Int. J. Plast. 21 (5) (2005) 981–1007.

[18] M. Moattari, I. Sattari-Far, I. Persechino, N. Bonora, Prediction of fracture toughness in ductile-to-brittle transition region using combined CDM and Beremin models, Mater. Sci. Eng.: A 657 (2016) 161–172.

[19] C. Miehe, M. Hofacker, L.M. Schaenzel, F. Aldakheel, Phase field modeling of fracture in multi-physics problems. Part ii. Coupled brittle-to-ductile failure criteria and crack propagation in thermo-elastic–plastic solids, Comput. Methods Appl. Mech. Eng. 294 (2015) 486–522.

[20] M. Ambati, L. De Lorenzis, Phase-field modeling of brittle and ductile fracture in shells with isogeometric NURBS-based solid-shell elements, Comput. Methods Appl. Mech. Eng. (2016).

[21] K. Arimoto, F. Ikuta, T. Horino, S. Tamura, M. Narazaki, Y. Mikita, Preliminary study to identify criterion for quench crack prevention by computer simulation, Cailiao Rechuli Xuebao/Trans. Mater. Heat Treat. 25 (5) (2004) 486–493.

[22] K. Arimoto, Simulation of steels prone to quench cracking, in: J. Dossett, G. Totten (Eds.), ASM Handbook, Heat Treating of Irons and Steels, vol. 4D, ASM International, Materials Park, OH, 2014, p. 014.

[23] G. Totten, C. Bates, N. Clinton, Residual stress, distortion and cracking, in: Handbook of Quenchants and Quenching Technology, ASM International, Materials Park, OH, 1993, p. 993.

[24] R. Blackwood, L. Jarvis, D. Hoffman, G. Totten, Conditions leading to quench cracking other than severity of quench, in: R. Wallis, H. Walton (Eds.), Heat Treating, Including the Liu Dai Memorial Symposium, Proc. of the 18th Conf., ASM International, 1998, pp. 575–585.

[25] G. Totten, M. Narazaki, R. Blackwood, L. Jarvis, Failures related to heat treating operations, in: W. Becker, R. Shipley (Eds.), ASM Handbook, Failure Analysis and Prevention, vol. 11, ASM International, Materials Park, OH, 2002, pp. 192–223.

[26] F. Uchida, S. Goto, R. Shindo, S. Nagata, Analysis of quenching crack generation in low alloy cast steel by using heat treatment simulation, J. Jpn. Foundry Eng. Soc. 77 (2005) 437–444.

[27] A. Sugianto, M. Narazaki, M. Kogawara, A. Shirayori, Failure analysis and prevention of quench crack of eccentric holed disk by experimental study and computer simulation, Eng. Fail. Anal. 16 (1) (2009) 70–84.

[28] D. Gallina, Finite element prediction of crack formation induced by quenching in a forged valve, Eng. Fail. Anal. 18 (8) (2011) 2250–2259.

[29] M.S. Qidwai, A.C. Lewis, A.B. Geltmacher, Using image-based computational modeling to study microstructure–yield correlations in metals, Acta Mater. 57 (14) (2009) 4233–4247.

[30] S. Katani, S. Ziaei-Rad, N. Nouri, N. Saeidi, J. Kadkhodapour, N. Torabian, et al., Microstructure modelling of dual-phase steel using SEM micrographs and Voronoi polycrystal models, Metallogr. Microstruct. Anal. 2 (3) (2013) 156–169.

[31] Y.J. Huang, Z.J. Yang, G.H. Liu, X.W. Chen, An efficient FE-SBFE coupled method for mesoscale cohesive fracture modelling of concrete, Comput. Mech. 58 (4) (2016) 635–655.

[32] D. Said Schicchi, F. Hoffmann, M. Hunkel, T. Lübben, Numerical and experimental investigation of the mesoscale fracture behavior of quenched steels, Fatigue Fract. Eng. Mater. Struct. 40 (4) (2017) 556–570.

[33] D. Said Schicchi, A. Caggiano, T. Lübben, M. Hunkel, F. Hoffmann, On the mesoscale fracture initiation criterion of heterogeneous steels during quenching, Mater. Perform. Characteriz. 6 (1) (2017) 80–104.

[34] D.P. Koistinen, R.E. Marburger, A general equation prescribing extent of austenite-martensite transformation in pure Fe-C alloys and plain carbon steels, Acta Metall. 7 (1959) 59–60.

[35] C. Simsir, C. Gür, Simulation of quenching, in: B. Liscic, H. Tensi, L. Canale, G.E. Totten (Eds.), Quenching Theory and Technology, second ed., CRC Press, Taylor & Francis Group, 2010, pp. 605–667 (Chapter 17) ISBN 9780849392795.

[36] J. Leblond, Mathematical modelling of transformation plasticity in steels II: coupling with strain hardening phenomena, Int. J. Plast. 5 (6) (1989) 573–591.

[37] P. Åkerström, G. Bergman, M. Oldenburg, Numerical implementation of a constitutive model for simulation of hot stamping, Modell. Simul. Mater. Sci. Eng. 15 (2) (2007) 105.

[38] K. Willam, I. Rhee, B. Shing, Interface damage model for thermomechanical degradation of heterogeneous materials, Comput. Methods Appl. Mech. Eng. 193 (30–32) (2004) 3327–3350.

[39] A. Caggiano, D. Said Schicchi, A thermo-mechanical interface model for simulating the bond behaviour of FRP strips glued to concrete substrates exposed to elevated temperature, Eng. Struct. 83 (2015) 243–251.

[40] Sonderforschungsbereich 570 Distortion Engineering. <http://www.sfb570.uni-bremen.de>.

[41] C. Acht, M. Dalgic, F. Frerichs, M. Hunkel, A. Irretier, T. Lübben, et al., Ermittlung der Materialdaten zur Simulation des Durchhaertens von Komponenten aus 100Cr6, Teil 1. HTM J. Heat Treatm. Mat. 63 (5) (2008) 234–244.

[42] C. Acht, M. Dalgic, F. Frerichs, M. Hunkel, A. Irretier, T. Lübben, et al., Ermittlung der Materialdaten zur Simulation des Durchhaertens von Komponenten aus 100Cr6. Teil 2, HTM J. Heat Treatm. Mat. 63 (6) (2008) 362–371.

[43] C. Zhou, B. Xiao, J. Feng, J. Xing, X. Xie, Y. Chen, et al., First principles study on the elastic properties and electronic structures of (Fe, Cr)3C, Comput. Mater. Sci. 45 (2009) 986–992.

[44] J. Epp, H. Surm, O. Kessler, T. Hirsch, In situ X-Ray phase analysis and computer simulation of carbide dissolution of ball bearing steel at different austenitizing temperatures, Acta Mater. 55 (17) (2007) 5959–5967.

[45] J. Epp, H. Surm, O. Kessler, T. Hirsch, In-situ X-ray investigations and computer simulation during continuous heating of a ball bearing steel, Metall. Mater. Trans. A 38 (10) (2007) 2371–2378.

[46] F. Frerichs, S. Sander, T. Lübben, S. Schttenberg, U. Fritsching, Determination of heat transfer coefficients in high speed quenching processes, Mater. Perform. Characteriz. 3 (4) (2014) 163–183.

[47] D. Said, G. Belinato, G.S. Sarmiento, R.L.S. Otero, G.E. Totten, A. Gastón, et al., Comparison of oxidation stability and quenchant cooling curve performance of soybean oil and palm oil, J. Mater. Eng. Perform. 22 (7) (2013) 1929–1936.

[48] D. Said Schicchi, F. Hoffmann, F. Frerichs, A mesoscopic approach of the quench cracking phenomenon influenced by chemical inhomogeneities, Eng. Fail. Anal. 78 (2017) 67–86.

[49] D. Peric, E.A. de Souza Neto, R.A. Feijóo, M. Partovi, A.J.C. Molina, On micro-to-macro transitions for multi-scale analysis of non-linear heterogeneous materials: unified variational basis and finite element implementation, Int. J. Numer. Meth. Eng. 87 (1–5) (2011) 149–170.